

NUSTAR OBSERVATIONS OF HEAVILY OBSCURED QUASARS AT $z \sim 0.5$

G. B. LANSBURY¹, D. M. ALEXANDER¹, A. DEL MORO¹, P. GANDHI¹, R. J. ASSEF², D. STERN³, J. AIRD¹, D. R. BALLANTYNE⁴,
 M. BALOKOVIĆ⁵, F. E. BAUER^{6,7}, S. E. BOGGS⁸, W. N. BRANDT^{9,10}, F. E. CHRISTENSEN¹¹, W. W. CRAIG^{11,12}, M. ELVIS¹³,
 B. W. GREFENSTETTE⁵, C. J. HAILEY¹⁴, F. A. HARRISON⁵, R. C. HICKOX¹⁵, M. KOSS¹⁶, S. M. LAMASSA¹⁷, B. LUO^{9,10},
 J. R. MULLANEY¹, S. H. TENG¹⁸, C. M. URRY¹⁷, AND W. W. ZHANG¹⁹

¹ Department of Physics, University of Durham, South Road, Durham DH1 3LE, UK; g.b.lansbury@durham.ac.uk

² Núcleo de Astronomía de la Facultad de Ingeniería, Universidad Diego Portales, Av. Ejército Libertador 441, Santiago, Chile

³ Jet Propulsion Laboratory, California Institute of Technology, 4800 Oak Grove Drive, Mail Stop 169-221, Pasadena, CA 91109, USA

⁴ Center for Relativistic Astrophysics, School of Physics, Georgia Institute of Technology, Atlanta, GA 30332, USA

⁵ Cahill Center for Astrophysics, 1216 East California Boulevard, California Institute of Technology, Pasadena, CA 91125, USA

⁶ Instituto de Astrofísica, Facultad de Física, Pontificia Universidad Católica de Chile, Casilla 306, Santiago 22, Chile

⁷ Space Science Institute, 4750 Walnut Street, Suite 205, Boulder, CO 80301, USA

⁸ Space Sciences Laboratory, University of California, Berkeley, CA 94720, USA

⁹ Department of Astronomy and Astrophysics, 525 Davey Lab, The Pennsylvania State University, University Park, PA 16802, USA

¹⁰ Institute for Gravitation and the Cosmos, The Pennsylvania State University, University Park, PA 16802, USA

¹¹ DTU Space-National Space Institute, Technical University of Denmark, Elektrovej 327, DK-2800 Lyngby, Denmark

¹² Lawrence Livermore National Laboratory, Livermore, CA 94550, USA

¹³ Harvard-Smithsonian Center for Astrophysics, 60 Garden Street, Cambridge, MA 02138, USA

¹⁴ Columbia Astrophysics Laboratory, 550 W 120th Street, Columbia University, NY 10027, USA

¹⁵ Department of Physics and Astronomy, Dartmouth College, 6127 Wilder Laboratory, Hanover, NH 03755, USA

¹⁶ Institute for Astronomy, Department of Physics, ETH Zurich, Wolfgang-Pauli-Strasse 27, CH-8093 Zurich, Switzerland

¹⁷ Yale Center for Astronomy and Astrophysics, Physics Department, Yale University, P.O. Box 208120, New Haven, CT 06520-8120, USA

¹⁸ Observational Cosmology Laboratory, NASA Goddard Space Flight Center, Greenbelt, MD 20771, USA

¹⁹ NASA Goddard Space Flight Center, Greenbelt, MD 20771, USA

Received 2013 November 12; accepted 2014 February 10; published 2014 March 21

ABSTRACT

We present *NuSTAR* hard X-ray observations of three Type 2 quasars at $z \approx 0.4\text{--}0.5$, optically selected from the Sloan Digital Sky Survey. Although the quasars show evidence for being heavily obscured, Compton-thick systems on the basis of the 2–10 keV to [O III] luminosity ratio and multiwavelength diagnostics, their X-ray absorbing column densities (N_{H}) are poorly known. In this analysis, (1) we study X-ray emission at >10 keV, where X-rays from the central black hole are relatively unabsorbed, in order to better constrain N_{H} . (2) We further characterize the physical properties of the sources through broad-band near-UV to mid-IR spectral energy distribution analyses. One of the quasars is detected with *NuSTAR* at >8 keV with a no-source probability of $<0.1\%$, and its X-ray band ratio suggests near Compton-thick absorption with $N_{\text{H}} \gtrsim 5 \times 10^{23} \text{ cm}^{-2}$. The other two quasars are undetected, and have low X-ray to mid-IR luminosity ratios in both the low-energy (2–10 keV) and high-energy (10–40 keV) X-ray regimes that are consistent with extreme, Compton-thick absorption ($N_{\text{H}} \gtrsim 10^{24} \text{ cm}^{-2}$). We find that for quasars at $z \sim 0.5$, *NuSTAR* provides a significant improvement compared to lower energy (<10 keV) *Chandra* and *XMM-Newton* observations alone, as higher column densities can now be directly constrained.

Key words: galaxies: active – X-rays: galaxies

Online-only material: color figures

1. INTRODUCTION

Quasars are the sites of the most rapid black hole growth in the universe (Salpeter 1964; Soltan 1982). They represent the luminous end of the active galactic nucleus (AGN) population, often outshining their host galaxies. The first unobscured (“Type 1”) quasars were discovered over 50 yr ago (Schmidt 1963; Hazard et al. 1963), and more than 100,000 have now been spectroscopically identified (e.g., Véron-Cetty & Véron 2010; Pâris et al. 2012). For obscured (“Type 2”) quasars²⁰, the situation is not as advanced. Similar to the early Type 1 quasars, Type 2 quasars were initially identified from radio selection (e.g., Minkowski

1960), and over the following decades several hundred powerful “radio galaxies” (as radio-selected Type 2 quasars are typically called) were identified (for reviews, see McCarthy 1993; Miley & De Breuck 2008). However, it has only been in the past decade that radio-quiet Type 2 quasars have been found in large numbers. Such sources are generally identified on the basis of either their relatively hard X-ray spectral slopes (e.g., Norman et al. 2002; Stern et al. 2002), optical spectral features (e.g., Steidel et al. 2002; Zakamska et al. 2003), or mid-infrared (mid-IR) colors (e.g., Lacy et al. 2004; Stern et al. 2005). Importantly, mid-IR color selection of Type 2 quasars using the all-sky *Wide-Field Infrared Survey Explorer* (*WISE*; Wright et al. 2010) survey identifies several million Type 2 quasars, roughly down to the bolometric luminosity of the primary Sloan Digital Sky Survey (SDSS; York et al. 2000) Type 1 quasar spectroscopic survey (Stern et al. 2012; Assef et al. 2013; Donoso et al. 2013).

The exact nature of Type 2 quasars is still under debate. A simple extension of the orientation-driven unified model of AGNs (Antonucci 1993; Urry & Padovani 1995) to high

²⁰ We define Type 2 quasars as AGNs with $L_{2-10\text{keV}} \geq 10^{44} \text{ erg s}^{-1}$, X-ray absorbing column densities $N_{\text{H}} > 10^{22} \text{ cm}^{-2}$, and optical spectra that show narrow line emission without broad (H α or H β) components. This $L_{2-10\text{keV}}$ threshold is consistent with (1) the classical optical quasar definition, $M_B \leq -23$, when the α_{OX} relation of Steffen et al. (2006) and the composite quasar spectrum of Vanden Berk et al. (2001) are assumed; and (2) the $L_{X,*}$ value derived by Hasinger et al. (2005) for unobscured AGNs.

luminosities can account for their existence. However, there is also observational evidence for an evolutionary link to Type 1 quasars (e.g., Sanders et al. 1988; Hopkins et al. 2008). The importance of Type 2 quasars to the cosmic evolution of AGNs is further demonstrated by their requirement in models of the cosmic X-ray background (CXB; e.g., Treister & Urry 2005; Gilli et al. 2007; Treister et al. 2009). However, the observed X-ray properties of Type 2 quasars are poorly constrained at present. Consequently, the column density (N_H) distribution²¹ and Compton-thick²² fraction of quasars are poorly known, which has implications for both AGN and CXB models (e.g., Fabian et al. 2008; Draper & Ballantyne 2010).

To date, the largest sample of spectroscopically confirmed (radio-quiet) Type 2 quasars at $z \lesssim 1$ is that of Zakamska et al. (2003) and Reyes et al. (2008). Zakamska et al. (2003) selected 291 Type 2 quasars at redshift $0.2 \lesssim z \lesssim 0.8$ from the SDSS based on their optical properties: high [O III] $\lambda 5007$ line power and narrow emission lines. Reyes et al. (2008) used the same approach and more recent SDSS data to extend the sample to 887 objects. While X-ray selections of Type 2 quasars at $\lesssim 10$ keV are biased against the most heavily obscured sources (e.g., Maiolino et al. 1998), [O III] emission is mostly produced on ~ 100 pc scales and is thus relatively unaffected by nuclear obscuration, allowing larger numbers of the heavily obscured, X-ray-faint objects to be found. Following up [O III]-selected, rather than X-ray-selected, objects with X-ray observations thus gives a less biased estimate of the N_H distribution of AGNs (e.g., Risaliti et al. 1999).

The X-ray properties of the Zakamska et al. (2003) and Reyes et al. (2008) Type 2 quasar sample have been studied using *Chandra* and *XMM-Newton* observations (Ptak et al. 2006; Vignali et al. 2006, 2010; Jia et al. 2013). Vignali et al. (2006, 2010) measured column densities for a handful of sources through “direct” means (i.e., using X-ray spectroscopic analysis). The highest column densities measured in this manner were $N_H \approx 3 \times 10^{23} \text{ cm}^{-2}$. However, distant obscured quasars are X-ray-weak and in most cases direct constraints are not feasible. Instead, an “indirect” approach to estimating column densities can be used where the observed X-ray emission is compared with a proxy for intrinsic AGN power (e.g., the mid-IR continuum emission from hot dust or high-excitation emission lines; Bassani et al. 1999; Lutz et al. 2004; Heckman et al. 2005; Alexander et al. 2005, 2008; Cappi et al. 2006; Panessa et al. 2006; Meléndez et al. 2008; Gandhi et al. 2009; LaMassa et al. 2009, 2011; Gilli et al. 2010; Goulding et al. 2011). Vignali et al. (2006, 2010) were limited to indirect absorption constraints for the majority of their Type 2 quasar sample, and found that Compton-thick absorption (i.e., $N_H > 1.5 \times 10^{24} \text{ cm}^{-2}$) is required to explain the X-ray suppression in these sources in every case. To first order, there appears to be a bimodal N_H distribution for optically selected Type 2 quasars, with $\sim 40\%$ having $N_H = 10^{22}$ to $3 \times 10^{23} \text{ cm}^{-2}$ and $\sim 60\%$ being Compton-thick. This is interesting given that a continuous N_H distribution is measured for Type 2 Seyferts (e.g., Bassani et al. 1999; Risaliti et al. 1999; LaMassa et al. 2009, 2011), although the differences may be reconciled by considering the different methods used to estimate N_H (LaMassa et al. 2011). To better constrain the N_H distribution of Type 2 quasars, more robust identifications of Compton-thick absorption must be obtained through either (1) measurement of strong Fe K α emission, with EW ≥ 1 keV,

which results from the Fe K α line being viewed in reflection against a suppressed continuum (e.g., Ghisellini et al. 1994; Levenson et al. 2002); or (2) measurement of high column densities through spectroscopic analysis at high energies above the photoelectric absorption cutoff (i.e., above observed-frame 8 keV for $z \sim 0.5$ and $N_H \sim 10^{24} \text{ cm}^{-2}$), where X-ray emission is relatively unabsorbed.

The recent launch of the *Nuclear Spectroscopic Telescope Array* (*NuSTAR*; Harrison et al. 2013) will see a breakthrough in our understanding of heavily obscured AGNs and the CXB population in general. *NuSTAR* is the first orbiting observatory with the ability to focus high-energy ($\gtrsim 10$ keV) X-rays using grazing incidence optics. It provides a two orders of magnitude improvement in sensitivity and over an order of magnitude improvement in angular resolution over previous hard X-ray observatories. The high-energy range at which *NuSTAR* operates (3–79 keV) means that the intrinsic, unabsorbed emission of AGNs is observed for all but the most heavily obscured, Compton-thick objects. At $z \lesssim 1$, it is now possible to directly constrain column densities an order of magnitude higher than those achievable with *Chandra* and *XMM-Newton* alone (e.g., Luo et al. 2013).

In this paper, we present exploratory *NuSTAR* observations of three optically selected Type 2 quasars at $z \approx 0.4$ – 0.5 . All three have been identified as Compton-thick candidates in previous studies (Vignali et al. 2006, 2010; Jia et al. 2013). We use X-ray data from *NuSTAR*, *Chandra*, and *XMM-Newton*, and near-UV to mid-IR data from other observatories to determine the physical properties of the quasars. In particular, we use a combination of direct and indirect methods to constrain the absorbing column densities. The paper is organized as follows. Our sample selection is detailed in Section 2. We describe the observations, data reduction, and data analysis in Section 3. The main results regarding X-ray absorption constraints are presented in Section 4 and we summarize our main conclusions in Section 5. The cosmology adopted throughout this work is $(\Omega_M, \Omega_\Lambda, h) = (0.27, 0.73, 0.71)$.

2. SAMPLE SELECTION

First, we selected objects at $z \approx 0.4$ – 0.5 from the *Chandra* and *XMM-Newton* studies of SDSS-selected Type 2 quasars by Vignali et al. (2006, 2010) and Jia et al. (2013). Although the objects have narrow H β line emission, the H α line lies outside the SDSS spectral range at these redshifts. Therefore, we cannot rule out that these quasars are luminous versions of the Type 1.9 Seyferts that show evidence for a broad H α component but no broad H β component (Osterbrock 1981). Second, we selected quasars with low observed X-ray to [O III] luminosity ratios, $L_{2-10\text{keV}}/L_{[\text{O III}]}$ < 2.5. This threshold corresponds to a two orders of magnitude suppression of the observed X-ray luminosity, assuming the Mulchaey et al. (1994) relation between [O III] and intrinsic 2–10 keV flux (taking into account the variance of the relation), which is consistent with Compton-thick absorption. This is a conservative selection, since the Mulchaey et al. (1994) relation was calibrated for Type 2 Seyferts, and Type 2 quasars typically have larger X-ray to [O III] luminosity ratios (Netzer et al. 2006). Third, we made sub-selections of three quasars which show evidence for extreme obscuration on the basis of different diagnostics.

1. SDSS J001111.97+005626.3 ($z = 0.409$, $L_{2-10\text{keV}} = 3.1 \times 10^{42} \text{ erg s}^{-1}$, $L_{[\text{O III}]} = 1.8 \times 10^{42} \text{ erg s}^{-1}$; Reyes et al. 2008; Jia et al. 2013) has a flat X-ray spectral slope

²¹ X-rays emitted from the immediate black hole environment are absorbed by circumnuclear gas, and thus provide constraints on N_H .

²² Compton-thick absorption is that with $N_H \geq \sigma_T^{-1} \approx 1.5 \times 10^{24} \text{ cm}^{-2}$.

Table 1
X-Ray Observation Log

Object Name	z	<i>NuSTAR</i>			Lower Energy X-Ray Observations			
		Observation ID	UT Date	Exposure	Observatory	Observation ID	UT Date	Exposure
(1)	(2)	(3)	(4)	(5)	(6)	(7)	(8)	(9)
SDSS J001111.97+005626.3	0.409	60001065002	2013 Jan 27	18.3 ks	<i>XMM-Newton</i>	0403760301	2006 Jul 10	25.7 ks
SDSS J005621.72+003235.8	0.484	60001061002	2013 Jan 27	21.9 ks	<i>Chandra</i>	7746	2008 Feb 08	9.91 ks
SDSS J115718.35+600345.6	0.491	60001071002	2012 Oct 28	21.7 ks	<i>Chandra</i>	5698	2005 Jun 03	6.97 ks

Notes. (1) Full SDSS object name. (2) Redshift. (3) and (4) *NuSTAR* observation ID and start date. (5) Net on-axis *NuSTAR* exposure time. This value applies to both FPMA and FPMB. (6) Lower energy X-ray observatory data used (*Chandra* or *XMM-Newton*). (7)–(9) *Chandra* or *XMM-Newton* observation ID, observation start date, and net on-axis exposure time, corrected for flaring and bad events.

at observed-frame 0.3–10 keV ($\Gamma = 0.6^{+1.17}_{-1.15}$; Jia et al. 2013), which suggests that the X-ray emission is rising steeply toward high energies (>10 keV). Unlike the other two quasars, there is no mid-IR spectroscopy available.

2. SDSS J005621.72+003235.8 ($z = 0.484$, $L_{2-10\text{ keV}} = 8.9 \times 10^{41} \text{ erg s}^{-1}$, $L_{[\text{O III}]} = 6.8 \times 10^{42} \text{ erg s}^{-1}$; Reyes et al. 2008; Vignali et al. 2010) has the deepest 9.7 μm silicate (Si) absorption of the sample of Type 2 quasars observed with *Spitzer*-IRS in Zakamska et al. (2008). Such strong Si features are typically found in Compton-thick AGNs (e.g., Shi et al. 2006; Georgantopoulos et al. 2011a; Goulding et al. 2012).
3. SDSS J115718.35+600345.6 ($z = 0.491$, $L_{2-10\text{ keV}} < 1.5 \times 10^{42} \text{ erg s}^{-1}$, $L_{[\text{O III}]} = 1.6 \times 10^{43} \text{ erg s}^{-1}$; Reyes et al. 2008; Vignali et al. 2010) is the most luminous quasar in the Vignali et al. (2010) sample at mid-IR wavelengths, but is undetected by *Chandra* (Vignali et al. 2006). The extremely low X-ray to mid-IR luminosity ratio is likely due to Compton-thick absorption (Vignali et al. 2010). The *Spitzer*-IRS spectrum for this source shows it to be quasar-dominated at mid-IR wavelengths, but that it also hosts ultraluminous star formation [$\log(L_{\text{SF}}/L_{\odot}) = 12.3$, Zakamska et al. 2008]. There is no evidence for significant Si-absorption; however, $\approx 50\%$ of the best-studied, Compton-thick AGNs do not have significant Si-absorption (e.g., Goulding et al. 2012).

3. *NuSTAR* AND MULTIWAVELENGTH DATA

In our analysis of the three Type 2 quasars, we used *NuSTAR* observations in conjunction with lower energy X-ray observations from *Chandra* and *XMM-Newton*, and near-UV to mid-IR data primarily from large-area public surveys. Hereafter we refer to the quasars using abbreviated SDSS object names.

3.1. *NuSTAR* Observations

NuSTAR consists of two co-aligned X-ray telescopes (focal length = 10.14 m) which use grazing incidence optics to focus hard X-rays (3–79 keV) onto two focal plane modules (FPMs A and B; Harrison et al. 2013). Each FPM provides a $\approx 12' \times 12'$ field of view at 10 keV, and a pixel size of $2''.46$. The *NuSTAR* point-spread function (PSF) is characterized by a FWHM of $18''$, and a half-power diameter of $58''$. The astrometric accuracy for bright X-ray sources is $\pm 8''$ (90% confidence; Harrison et al. 2013).

The Type 2 quasars, SDSS J0011+0056, SDSS J0056+0032, and SDSS J1157+6003, were observed by *NuSTAR* with nominal exposure times of 19.6 ks, 23.5 ks, and 23.3 ks, respectively. Details of the observations, including net exposure times, are

provided in Table 1. We processed the data using the *NuSTAR* Data Analysis Software (NuSTARDAS) v. 1.3.0. Calibrated and cleaned event files were produced using the NUPipeline script and the *NuSTAR* CALDB 20131007 release with the standard filter flags.

3.1.1. Photometry and Source Detection

To characterize the high-energy X-ray emission and determine whether sources are detected, we performed photometry in the observed-frame 3–24 keV, 3–8 keV, and 8–24 keV bands for both of the *NuSTAR* FPMs following Alexander et al. (2013). We avoided using photons above 24 keV, where the drop in effective area and the prominent background features (see Figures 2 and 10 of Harrison et al. 2013, respectively) hinder the analysis of faint X-ray sources such as Type 2 quasars. We split the *NuSTAR* event files into individual band images using DMCOPY, part of the *Chandra* Interactive Analysis Observations software (CIAO, v4.4; Fruscione et al. 2006).²³ We extracted the gross source counts (S) from a $45''$ radius aperture centered on the SDSS position. For a source at the *NuSTAR* aim point, and for the energy range (3–24 keV) and spectral slopes ($\Gamma = 0.6\text{--}1.8$) used in this study, this aperture encloses $\approx 65\%$ of the full PSF energy. We extracted the background counts (B) from an annulus with an inner radius $90''$ from the source and an outer radius $150''$ from the source, which allowed the local background to be sampled while minimizing contamination from the source. To obtain the background counts in the source extraction region (B_{src}), we multiplied B by the area scaling factor between the source and background regions (A_S/A_B). Net source counts were calculated as $S - B_{\text{src}}$, and corresponding 68.3% confidence level uncertainties were taken as $\sqrt{S + B(A_S/A_B)^2}$. For non-detections, we calculated 99.7% confidence level upper limits using the Bayesian method of Kraft et al. (1991). The *NuSTAR* photometry is given in Table 2.

To test whether the quasars are detected in the individual *NuSTAR* band images, we looked for significant source signals at their SDSS positions. We assumed binomial statistics and calculated false probabilities, or “no-source” probabilities (P), using the following equation:

$$P(x \geq S) = \sum_{x=S}^T \frac{T!}{x!(T-x)!} p^x (1-p)^{T-x}, \quad (1)$$

where $T = S + B$ and $p = 1/(1 + B/B_{\text{src}})$. P is the probability that, assuming there is no source at the SDSS position, the measured gross counts in the source aperture (S) are purely due to a background fluctuation (Weisskopf et al. 2007).

²³ <http://cxc.harvard.edu/ciao/index.html>

Table 2
X-Ray Photometry

Object Name (1)	Net Counts (FPMA)			Net Counts (FPMB)			Flux (<i>NuSTAR</i>)			Flux (Other)
	3–24	3–8	8–24	3–24	3–8	8–24	3–24	3–8	8–24	3–8
0011+0056	17.5 ± 7.7	<16.3	16.8 ± 6.4	<24.7	<18.3	<19.7	0.99	<0.74	1.32	0.18
0056+0032	<19.1	<10.9	<20.9	<23.5	<17.8	<19.6	<1.14	<0.52	<1.58	<0.16
1157+6003	<31.4	<16.6	<29.1	<23.3	<20.0	<17.7	<1.35	<0.63	<1.68	<0.22

Notes. (1) Abbreviated SDSS object name. The “SDSS J” prefix and all R.A. and decl. digits after the first four have been truncated. (2) and (3) Net source counts in the observed-frame 3–24, 3–8, and 8–24 keV bands for FPMA and FPMB, respectively. 68.3% confidence level uncertainties, and 99.7% confidence level upper limits are given. (4) Aperture-corrected *NuSTAR* flux in units of 10^{-13} erg s $^{-1}$ cm $^{-2}$ (for a power-law model with $\Gamma = 1.8$), in the observed-frame 3–24, 3–8, and 8–24 keV bands. For SDSS J0011+0056, the fluxes are for FPMA only, while for SDSS J0056+0032 and SDSS J1157+6003, the fluxes are averaged over FPMA and FPMB. (5) Aperture-corrected observed-frame 3–8 keV flux in units of 10^{-13} erg s $^{-1}$ cm $^{-2}$ (for a power-law model with $\Gamma = 1.8$), as measured using lower-energy X-ray data. *XMM-Newton* data have been used for SDSS J0011+0056, and *Chandra* data have been used for SDSS J0056+0032 and SDSS J1157+6003. 99.7% confidence level upper limits are given.

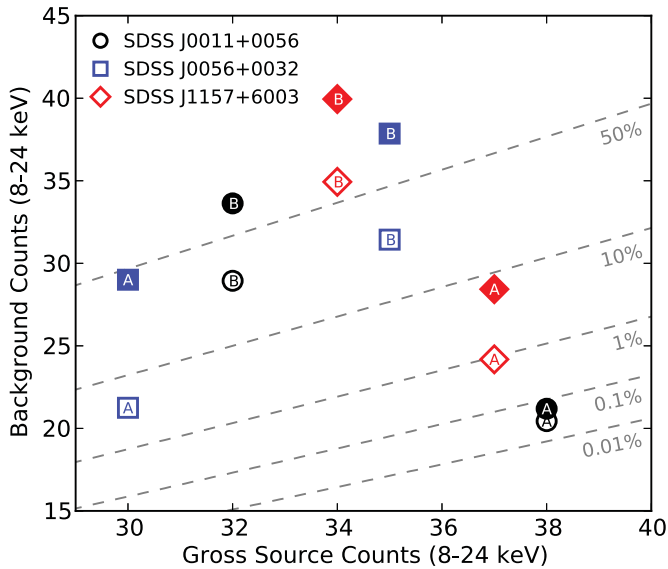


Figure 1. Gross source counts (S) vs. scaled background counts (B_{src}) at observed-frame 8–24 keV for SDSS J0011+0056, SDSS J0056+0032, and SDSS J1157+6003 (circles, squares, and diamonds, respectively). Background counts were measured using two approaches: direct measurement from the *NuSTAR* images (filled symbols), and from model background maps (empty symbols). The A and B labels correspond to FPMA and FPMB, respectively. The dashed lines indicate Poisson no-source probabilities. There is one significant detection: SDSS J0011+0056 is detected with FPMA.

(A color version of this figure is available in the online journal.)

Given that the three Type 2 quasars are faint at 3–8 keV (see Table 2 for *Chandra* and *XMM-Newton* fluxes and upper limits), and likely have flat X-ray spectra with emission rising steeply to higher energies, *NuSTAR* is most likely to detect the sources above 8 keV (observed-frame). At these energies, *Chandra* and *XMM-Newton* have little to no sensitivity. In Figure 1, we show the S and B_{src} values measured with *NuSTAR* for the 8–24 keV band (filled symbols), and the no-source probabilities to which they correspond (dashed lines).²⁴ For the purposes of this figure, Poisson statistics have been assumed; for our sources, B is large and the Poisson integral thus provides a good approximation of Equation (1) (Weisskopf et al. 2007). Taking binomial no-source probabilities greater than 1% to indicate non detections, neither SDSS J0056+0032 nor SDSS J1157+6003 are detected in either FPM. SDSS J0011+0056, on the other hand, is detected

in FPMA with a binomial no-source probability of 0.093%.²⁵ The *NuSTAR* image corresponding to this detection is shown in Figure 2. The source is not detected in FPMB, which has higher background noise relative to FPMA for this observation; indeed, the net source counts for FPMA are consistent with the upper limit for FPMB (see Table 2). SDSS J0011+0056 is also weakly detected in the 3–24 keV band for FPMA, with a binomial no-source probability of 0.58%. Aside from this, none of the quasars are detected in the 3–8 keV and 3–24 keV bands.

The no-source probability is sensitive to the background region sampled. To partially address this we also measured the background from model background maps produced using NUSKYBGD (D. R. Wik et al., in preparation), summing counts within the 45'' radius source aperture. These measurements are shown as empty symbols in Figure 1. SDSS J0011+0056 is still detected in FPMA using this approach, with a no-source probability of 0.033% at 8–24 keV.

3.1.2. Flux Calculation

For each *NuSTAR* energy band we determined the conversion factor between net count rate and source flux using XSPEC v12.8.1j (Arnaud 1996), taking into account the response matrix file (RMF) and ancillary response file (ARF) for each FPM. We assumed a power-law model with $\Gamma = 1.8$, consistent with that found for AGNs at observed-frame 3–24 keV (Alexander et al. 2013). We corrected fluxes to the 100% encircled-energy fraction of the PSF. The *NuSTAR* fluxes are given in Table 2.

For the *NuSTAR*-detected quasar, SDSS J0011+0056, we measure an observed-frame 8–24 keV flux of 1.32×10^{-13} erg s $^{-1}$ cm $^{-2}$. This value is consistent with extrapolations from the *XMM-Newton* 0.5–10 keV count rate given the photon index constraints of Jia et al. (2013), $\Gamma = 0.6^{+1.17}_{-1.15}$, and assuming a simple unabsorbed power-law model. Additionally, as we later show in Section 4.2, our X-ray flux measurement for SDSS J0011+0056 is consistent with that expected from its 6 μ m luminosity, which is assumed to result from the reprocessing of AGN emission by obscuring dust.

3.2. Lower Energy X-Ray Data

For SDSS J0011+0056 we used the archival *XMM-Newton* EPIC observation, first published in Jia et al. (2013). We analyzed the Pipeline Processing System data products for

²⁴ We avoid overplotting the errors for individual S and B_{src} measurements, since these are not used in the calculation of no-source probabilities.

²⁵ We note that in this case, using a 50'' (as opposed to 45'') source aperture results in a lower no-source probability of 0.049%.

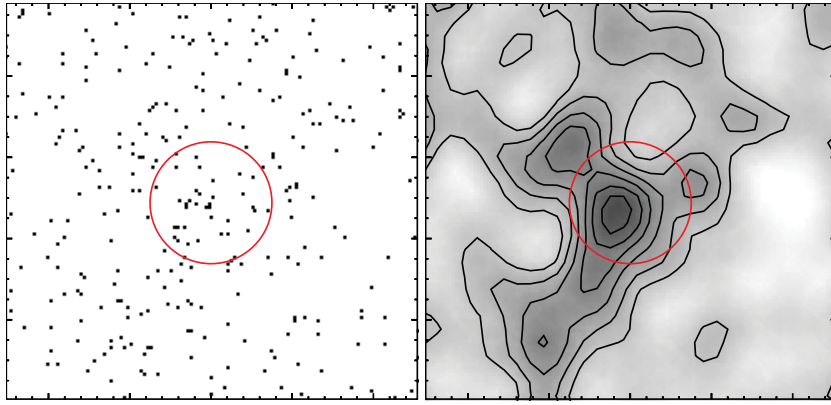


Figure 2. *NuSTAR* FPMA 8–24 keV image centered on the SDSS position of SDSS J0011+0056. Left panel: unsmoothed image. Right panel: image smoothed with a Gaussian of radius 14 pixels ($34''/5$), and with overlaid contours of constant pixel values. The smoothing and contours are for display purposes only. A $45''$ radius aperture is shown (red circle), centered on the SDSS position. The horizontal and vertical axes are right ascension (R.A.) and declination (decl.), respectively. The major ticks indicate 1 arcmin offsets.

(A color version of this figure is available in the online journal.)

this observation using the *Science Analysis Software*²⁶ (SAS v.12.0.1). The MOS1 and MOS2 data were coadded with the SAS task EPICSPECCOMBINE. The PN data were excluded, since SDSS J0011+0056 is close to a chip gap. The source counts were extracted from a $15''$ radius aperture and the background counts were extracted using an $80''$ radius source-free aperture, selected to sample the local background while avoiding chip gaps and nearby serendipitous sources. We used XSPEC to convert from count rate to flux, assuming a power-law model with $\Gamma = 1.8$ and using the *XMM-Newton* RMF and ARF. Throughout this work, we neglect the cross-calibration constants between MOS and *NuSTAR* as the current best estimates are $\sim 7 \pm 5\%$ (K. K. Madsen et al., in preparation), and a change on this scale does not affect our results.

For SDSS J0056+0032 and SDSS J1157+6003, we used the archival *Chandra* observations, first published in Vignali et al. (2006, 2010). We reprocessed the data using CHANDRA_REPRO,²⁷ a CIAO pipeline, to create event files. The source counts were extracted from a $3''$ radius aperture, and the background counts were extracted from an annulus with an inner radius $10''$ from the source and an outer radius $30''$ from the source. As SDSS J0056+0032 and SDSS J1157+6003 are non-detections at observed-frame 3–8 keV, we calculated 99.7% confidence level upper limits for the source counts using the Bayesian method of Kraft et al. (1991). To calculate fluxes, we converted from *Chandra* count rates with the HEASARC tool WebPIMMs²⁸ (v4.6b) assuming a power-law model with $\Gamma = 1.8$, and corrected to the 100% encircled-energy fraction of the PSF.

As the Type 2 quasars are faint at X-ray wavelengths, we are unable to fit the spectra accurately. For instance, SDSS J0011+0056 is detected with *XMM-Newton*, but using the combined MOS1+MOS2 data we only extract 5.6 and 20.6 net source counts in the observed-frame 0.5–3 keV and 3–8 keV bands, respectively. We list the *Chandra* and *XMM-Newton* 3–8 keV fluxes and upper limits in Table 2.

3.3. Near-UV to Mid-IR Data and SED Decomposition

To investigate the multiwavelength properties of the three Type 2 quasars, in particular the mid-IR emission from the

AGN, we collected photometric data at 0.3–30 μm (i.e., at near-UV through mid-IR wavelengths). We used imaging data from public large-area surveys, primarily the SDSS (York et al. 2000), the UKIRT Infrared Deep Sky Survey (UKIDSS; Lawrence et al. 2007), and the *WISE* all-sky survey (Wright et al. 2010). Additionally, for SDSS J0056+0032 and SDSS J1157+6003, we used *Spitzer* photometry from the *Spitzer* Enhanced Imaging Products Source List.²⁹ The photometric data set, not corrected for Galactic extinction, is provided in Table 3. We note that since the observations are not contemporaneous, AGN variability may affect the spectral energy distribution (SED) analysis at longer wavelengths, where the AGN is bright with respect to the host galaxy.

We used the near-UV through mid-IR photometric data to produce broad-band SEDs for our sample. We modeled the SEDs using the Assef et al. (2010) 0.03–30 μm empirical low-resolution AGN and galaxy templates. Each SED was modeled as a best-fit combination of an elliptical, a spiral and an irregular galaxy component, plus an AGN. We refer the reader to Assef et al. (2008, 2010, 2013) for further details. In Figure 3, we present the SEDs and best-fitting model solutions. For SDSS J1157+6003, we also show the *IRAS* 60 μm flux measured by Zakamska et al. (2004, green data point in Figure 3), which lies beyond the wavelength range of the galaxy templates and was therefore excluded from the SED modeling. The data point is consistent with a simple extrapolation of the best-fitting model from shorter wavelengths. Zakamska et al. (2004) also detect SDSS J0056+0032 at 60 μm , but at a low significance level (80% confidence). In Table 3, we provide the best-fitting parameters \hat{a} (the fractional contribution from the AGN component to the 0.1–30 μm emission after correction for dust reddening; Assef et al. 2010) and $L_{6\mu\text{m}}$ (the luminosity of the AGN component at rest-frame 6 μm after correction for dust reddening; νL_ν). The uncertainties on \hat{a} and $L_{6\mu\text{m}}$ are standard deviations, derived from the Monte Carlo re-sampling of the data according to the photometric uncertainties. Both parameters are well constrained.³⁰ Since our SED modeling uses a single AGN template, it does not account for the fact that AGNs show a range of heated dust emission relative to the bolometric emission of the accretion disk. For instance, assuming the

²⁶ <http://xmm.esa.int/sas/>

²⁷ http://cxc.harvard.edu/ciao/ahelp/chandra_repro.html

²⁸ <http://heasarc.gsfc.nasa.gov/Tools/w3pimms.html>

²⁹ <http://irsa.ipac.caltech.edu/data/SPITZER/Enhanced/Imaging/>

³⁰ Constraining \hat{a} and $L_{6\mu\text{m}}$ is the primary purpose of our SED analysis. We do not read deeply into the host-galaxy properties of the best fitting solutions.

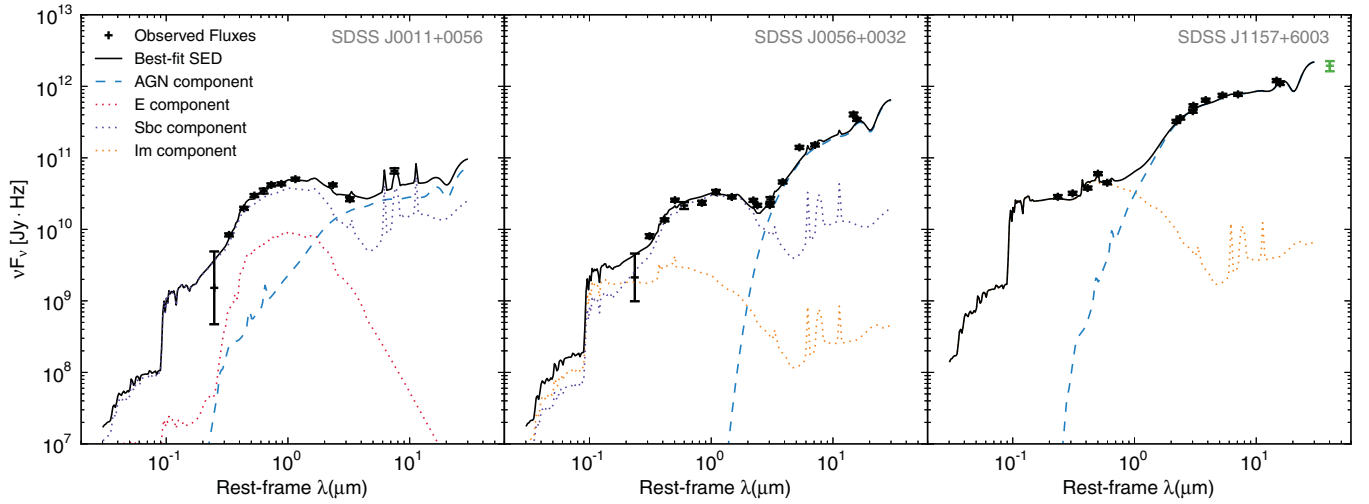


Figure 3. Near-UV to mid-IR SEDs for the three Type 2 quasars. The best-fitting model solutions (black line) were achieved using the AGN (blue dashed line) and galaxy (elliptical: red dotted line; spiral: purple dotted line; irregular: orange dotted line) templates of Assef et al. (2010). The photometric data (black data points) and best-fitting parameters are given in Table 3. The *IRAS* 60 μm flux for SDSS J1157+6003 (green data point) was not used in the SED decomposition.

(A color version of this figure is available in the online journal.)

Table 3
Near-ultraviolet to Mid-infrared Source Properties

Object Name ^a	0011+0056	0056+0032	1157+6003
<i>u</i> (0.355 μm) ^b	23.51 \pm 0.99	23.25 \pm 0.71	20.53 \pm 0.06
<i>g</i> (0.468 μm) ^b	21.50 \pm 0.05	21.60 \pm 0.069	20.10 \pm 0.01
<i>r</i> (0.616 μm) ^b	20.26 \pm 0.05	20.72 \pm 0.05	19.61 \pm 0.02
<i>i</i> (0.748 μm) ^b	19.60 \pm 0.04	19.82 \pm 0.04	18.90 \pm 0.01
<i>z</i> (0.892 μm) ^b	19.25 \pm 0.09	19.81 \pm 0.12	19.02 \pm 0.05
<i>Y</i> (1.03 μm) ^c	18.25 \pm 0.04
<i>J</i> (1.25 μm) ^c	17.70 \pm 0.03	18.42 \pm 0.07	...
<i>H</i> (1.63 μm) ^c	16.81 \pm 0.04	17.31 \pm 0.07	...
<i>K</i> (2.20 μm) ^c	...	16.64 \pm 0.05	...
<i>WISE</i> (3.4 μm) ^d	14.94 \pm 0.04	15.53 \pm 0.05	12.78 \pm 0.02
<i>WISE</i> (4.6 μm) ^d	14.45 \pm 0.07	14.51 \pm 0.08	11.24 \pm 0.02
<i>WISE</i> (12 μm) ^d	10.62 \pm 0.09	9.77 \pm 0.05	8.0 \pm 0.02
<i>WISE</i> (22 μm) ^d	...	6.55 \pm 0.07	5.37 \pm 0.03
<i>Spitzer</i> (3.6 μm) ^e	...	0.173 \pm 0.003	2.860 \pm 0.009
<i>Spitzer</i> (4.5 μm) ^e	...	0.220 \pm 0.003	4.511 \pm 0.010
<i>Spitzer</i> (5.8 μm) ^e	...	0.591 \pm 0.009	8.215 \pm 0.017
<i>Spitzer</i> (8.0 μm) ^e	...	2.474 \pm 0.016	13.165 \pm 0.022
<i>Spitzer</i> (24 μm) ^f	...	18.088 \pm 0.058	57.318 \pm 0.062
<i>IRAS</i> (60 μm) ^g	260.0 \pm 46.0
\hat{a} ^h	0.590 \pm 0.029	0.946 \pm 0.003	0.977 \pm 0.001
$L_{6\mu\text{m}}$ ^h	1.14 \pm 0.15	15.19 \pm 0.60	51.44 \pm 1.12

Notes.

^a Abbreviated SDSS object name.

^b SDSS DR7 Fiber magnitudes in the AB sinh system.

^c UKIDSS DR9 2'' diameter aperture magnitudes in the Vega system.

^d *WISE* profile-fit magnitudes in the Vega system.

^e *Spitzer* 3'' diameter aperture flux densities in units of mJy.

^f *Spitzer* PSF-fit flux densities in units of mJy.

^g *IRAS* flux density in units of mJy (Zakamska et al. 2004). This data point was not used in the SED modeling.

^h Best-fit parameters (corrected for dust reddening) from the SED decomposition described in Section 3.3: \hat{a} is the fractional contribution of the AGN to the 0.1–30 μm emission; $L_{6\mu\text{m}}$ is the rest-frame 6 μm luminosity (νL_ν) of the AGN in units of $10^{44} \text{ erg s}^{-1}$. The uncertainties are standard deviations, derived from the Monte Carlo re-sampling of the photometric data.

distribution of quasar covering factors found by Roseboom et al. (2013) would introduce an additional uncertainty to the 6 μm luminosities of $\approx \pm 0.5 L_{6\mu\text{m}}$. Our three Type 2 quasars have high \hat{a} values, which indicates that they are AGN-dominated at

0.1–30 μm . For SDSS J0056+0032 and SDSS J1157+6003, this is in agreement with the *Spitzer*-IRS spectroscopy of Zakamska et al. (2008), which shows the sources to be AGN-dominated at mid-IR wavelengths (for SDSS J0011+0056 there is no mid-IR spectroscopy available).

4. RESULTS

The three Type 2 quasars in this work bear the signatures of heavily obscured, Compton-thick AGNs based on multi-wavelength diagnostics (see Section 2 of this work; Zakamska et al. 2008; Vignali et al. 2010; Jia et al. 2013). Here we present the results of our analysis, which is aimed at assessing the prevalence of extreme absorption in these systems.

X-rays provide a direct measure of AGN emission that has been subject to circumnuclear absorption. As such, the characterization of X-ray spectra is necessary to obtain reliable estimates of absorbing column densities (N_{H}).³¹ For SDSS J0011+0056, we detect X-rays over the observed-frame 3–24 keV energy range, and for SDSS J0056+0032 and SDSS J1157+6003, we place upper limits on the 3–24 keV emission (see Table 2). As the quasars are at best weak detections at 3–24 keV, detailed modeling of their X-ray spectra is unfeasible. For SDSS J0011+0056, we characterize the observed-frame 3–24 keV X-ray spectrum using the ratio of hard (8–24 keV) to soft (3–8 keV) emission, which provides a direct absorption constraint (see Section 4.1). For the remaining two quasars, we are limited to indirect absorption constraints from the comparison of the observed X-ray emission with the intrinsic X-ray emission implied by infrared measurements (see Section 4.2).

4.1. Direct (X-Ray) Absorption Constraints

SDSS J0011+0056 is detected with *NuSTAR* in the 8–24 keV band, but not in the 3–8 keV band. We measure a 99.7% confidence level lower limit for the *NuSTAR* X-ray band ratio (i.e., the ratio of 8–24 keV counts to 3–8 keV counts), of >1.0 . In Figure 4, we show the *NuSTAR* band ratio against redshift for SDSS J0011+0056 and the first 10 sources detected

³¹ All N_{H} values in this section are line-of-sight column densities unless otherwise stated. In the MYTORUS model, N_{H} is related to the equatorial column density ($N_{\text{H,eq}}$) via Equation (1) in Murphy & Yaqoob (2009).

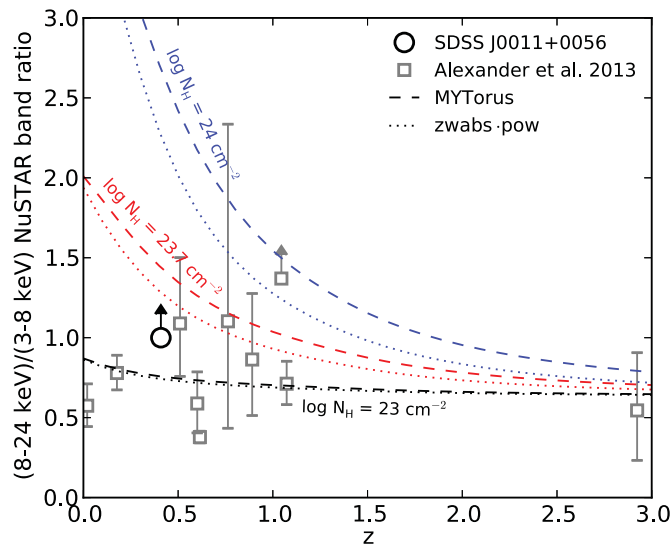


Figure 4. *NuSTAR* X-ray band ratio (8–24 keV to 3–8 keV counts ratio) against redshift for SDSS J0011+0056 (black circle), and the *NuSTAR*-detected sources in Alexander et al. (2013; gray squares). The dashed and dotted lines show band ratio predictions from MYTORUS and simple ZWABS-POW models, respectively, for a variety of column densities, and assuming a spectral slope of $\Gamma = 1.8$. Varying θ_{obs} makes a negligible difference to the MYTORUS tracks. Based on the 99.7% lower limit for the *NuSTAR* band ratio, SDSS J0011+0056 is consistent with being heavily obscured.

(A color version of this figure is available in the online journal.)

in the *NuSTAR* extragalactic survey (Alexander et al. 2013); the SDSS J0011+0056 band ratio is amongst the most extreme. We compare the band ratio with predictions from a simple absorbed power-law (ZWABS-POW) model and the MYTORUS model (Murphy & Yaqoob 2009), both of which are implemented in XSPEC. MYTORUS is a self-consistent physical model that is valid for the energy range 0.5–500 keV, and for column densities of $N_{\text{H}} = 10^{22}$ – 10^{25} cm^{-2} . It is more suitable than the ZWABS-POW model for column densities of $N_{\text{H}} \gtrsim 5 \times 10^{23} \text{ cm}^{-2}$, where a careful treatment of scattering and reflection is needed (for instance, see Figure 5). In the MYTORUS model, an obscuring torus reprocesses X-rays from a central source, and the resulting X-ray spectrum has both transmitted and scattered components. In the current implementation of MYTORUS, the half-opening angle of the obscuring medium is fixed to 60° (i.e., a covering factor of 0.5), a value inferred from the obscured AGN fraction of Seyfert galaxies. We note that a larger half-opening angle could be more appropriate in this study of Type 2 quasars, since the obscured AGN fraction is observed to decrease with luminosity (e.g., Ueda et al. 2003; Lusso et al. 2013). We assume a specific MYTORUS model with an intrinsic photon index of $\Gamma = 1.8$ (typical value for AGNs at observed-frame 3–24 keV; Alexander et al. 2013) and an inclination angle of $\theta_{\text{obs}} = 70^\circ$, referred to as *Model A* hereafter. Varying θ_{obs} between 65° and 90° , where 90° corresponds to an edge-on view through the equatorial plane of the torus, makes a negligible difference to the MYTORUS band ratio tracks in Figure 4. We avoid using θ_{obs} values close to 60° , below which the line-of-sight X-ray emission does not intercept the torus and the MYTORUS model therefore describes an unobscured AGN. As shown in Figure 4, the *NuSTAR* band ratio lower limit for SDSS J0011+0056 corresponds to an absorbing column density of $N_{\text{H}} \gtrsim 2.5 \times 10^{23} \text{ cm}^{-2}$. This implies heavy, but not necessarily Compton-thick, absorption.

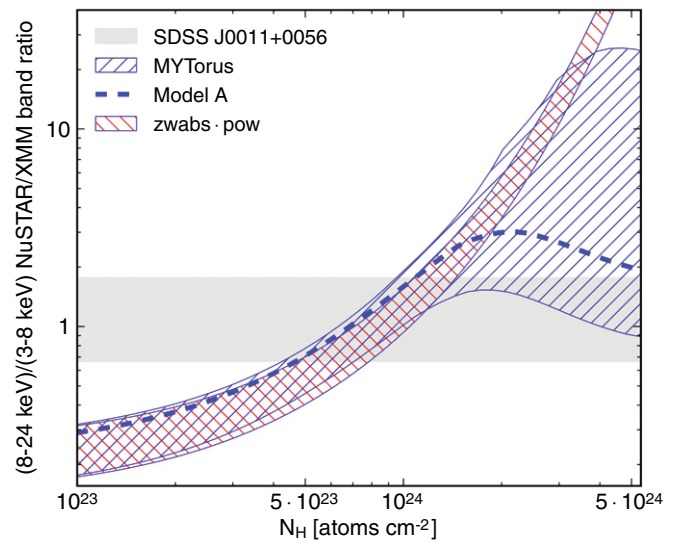


Figure 5. *NuSTAR/XMM-Newton* X-ray band ratio (*NuSTAR* 8–24 keV to *XMM-Newton* 3–8 keV count-rate ratio) against line-of-sight X-ray absorbing column density (N_{H}). The gray shaded area shows the 68.3% confidence level region for the observed band ratio of SDSS J0011+0056. The hashed regions show the range of band ratios predicted with MYTORUS (blue) and a simple ZWABS-POW model (red) for $z = 0.409$, and for a range of intrinsic photon indices ($1.7 < \Gamma < 2.3$). The MYTORUS region was computed for a range of inclination angles ($65^\circ < \theta_{\text{obs}} < 90^\circ$). According to these models, SDSS J0011+0056 is absorbed by $N_{\text{H}} \gtrsim 5 \times 10^{23} \text{ cm}^{-2}$. We also show band ratio predictions for a specific MYTORUS model with $\Gamma = 1.8$ and $\theta_{\text{obs}} = 70^\circ$ (*Model A*; dashed blue line); on the basis of *Model A*, SDSS J0011+0056 is absorbed by $N_{\text{H}} = (8.1^{+2.9}_{-3.4}) \times 10^{23} \text{ cm}^{-2}$.

(A color version of this figure is available in the online journal.)

Since *XMM-Newton* is more sensitive than *NuSTAR* at $<8 \text{ keV}$, we also measure an X-ray band ratio for SDSS J0011+0056 using the *XMM-Newton* 3–8 keV data and *NuSTAR* 8–24 keV data, which gives a *NuSTAR/XMM-Newton* band ratio of 1.2 ± 0.6 (68.3% confidence level). One limitation of the measurement is that we are unable to assess whether the X-ray emission of SDSS J0011+0056 has varied significantly in the $\sim 6.5 \text{ yr}$ between the *XMM-Newton* and *NuSTAR* observations; if the *XMM-Newton* count rate is relatively low, we overestimate the band ratio, and vice versa. In Figure 5, we compare the measured *NuSTAR/XMM-Newton* band ratio with predictions from the MYTORUS and ZWABS-POW models as a function of column density. We fixed the model redshifts to that of SDSS J0011+0056 ($z = 0.409$), used a range of intrinsic photon indices corresponding to those observed for unobscured AGNs ($1.7 < \Gamma < 2.3$; e.g., Mateos et al. 2010; Scott et al. 2011), and used a range of inclination angles in the MYTORUS model ($65^\circ < \theta_{\text{obs}} < 90^\circ$). The resulting tracks in Figure 5 suggest that SDSS J0011+0056 is absorbed by $N_{\text{H}} \gtrsim 5 \times 10^{23} \text{ cm}^{-2}$, which is consistent with the *NuSTAR* band ratio analysis (Figure 4). Assuming *Model A* ($\Gamma = 1.8$ and $\theta_{\text{obs}} = 70^\circ$), the observed *NuSTAR/XMM-Newton* band ratio for SDSS J0011+0056 implies a column density of $N_{\text{H}} = (8.1^{+2.9}_{-3.4}) \times 10^{23} \text{ cm}^{-2}$ (i.e., heavy, but not clearly Compton-thick, absorption is required to produce the observed 3–24 keV X-ray spectrum). This result is consistent with column density estimates from indirect methods, as shown in Section 4.2. For comparison, the highest column densities directly constrained by Vignali et al. (2006, 2010) in their $<10 \text{ keV}$ analysis of SDSS-selected Type 2 quasars are $N_{\text{H}} \approx 3 \times 10^{23} \text{ cm}^{-2}$.

The above N_{H} constraint for SDSS J0011+0056 must be treated with a degree of caution, since it depends on the assumed

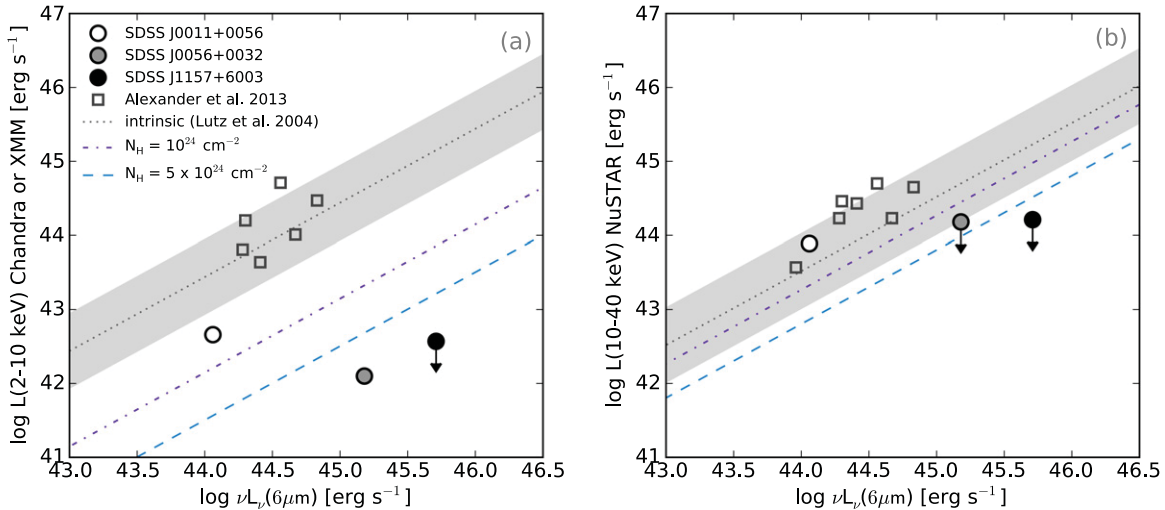


Figure 6. Rest-frame X-ray luminosity against rest-frame $6\mu\text{m}$ luminosity for (a) 2–10 keV luminosities calculated using *XMM-Newton* or *Chandra* data and (b) 10–40 keV luminosities calculated using *NuSTAR* data. The X-ray luminosities are not corrected for absorption. SDSS J0011+0056, SDSS J0056+0032, and SDSS J1157+6003 are shown as white, gray, and black circles, respectively. We compare with sources detected as part of the *NuSTAR* extragalactic survey (open squares; Alexander et al. 2013). We also compare with an intrinsic relation for 2–10 keV, calibrated using local AGNs (dotted line, with a shaded region indicating the scatter; Lutz et al. 2004). This relation has been extrapolated to the 10–40 keV band assuming $\Gamma = 1.8$, and to relations for AGNs absorbed by $N_{\text{H}} = 10^{24} \text{ cm}^{-2}$ (dash-dotted line) and $N_{\text{H}} = 5 \times 10^{24} \text{ cm}^{-2}$ (dashed line) assuming a MYTORUS model with $\Gamma = 1.8$ and $\theta_{\text{obs}} = 70^\circ$. If we assume that low X-ray luminosities are due to absorption, sources that lie below the $N_{\text{H}} = 10^{24} \text{ cm}^{-2}$ tracks may be Compton-thick.

(A color version of this figure is available in the online journal.)

X-ray spectral model. Here we assess the impact on our result of two spectral complexities, both of which are important in the case of Type 2 quasars. First, a soft “scattered” power law component is commonly observed for obscured AGNs which may be either nuclear emission scattered by hot gas (e.g., Turner et al. 1997), or “leakage” of nuclear emission due to partial covering (e.g., Vignali et al. 1998; Corral et al. 2011). Adding a scattered component which is 2% of the primary transmitted power law (a typical X-ray scattering fraction for Type 2 Seyferts; e.g., Turner et al. 1997) to *Model A*, we obtain a consistent result: $N_{\text{H}} > 4.9 \times 10^{23} \text{ cm}^{-2}$ (68.3% confidence level lower limit). Second, the absorbing medium may have a complex geometry (e.g., a clumpy torus) that requires the equatorial and line-of-sight column densities of the MYTORUS model ($N_{\text{H,eq}}$ and N_{H} , respectively) to be treated independently. Decoupling these two parameters in *Model A* and setting $N_{\text{H,eq}}$ to the maximum possible value of 10^{25} cm^{-2} yields a consistent result: $N_{\text{H}} = (7.7^{+2.8}_{-3.4}) \times 10^{23} \text{ cm}^{-2}$. Last, we emphasize that although MYTORUS is a relatively complex model, the N_{H} constraints do not differ significantly from those using a simple ZWABS-POW model in the Compton-thin regime (see Figure 5). We conclude that the inferred N_{H} for SDSS J0011+0056 does not change significantly with the assumed spectral model.

4.2. Indirect Absorption Constraints

The X-ray emission in heavily obscured AGNs is subject to significant absorption along the line of sight. The mid-IR emission, on the other hand, has been reprocessed by the dust obscuring the AGN and is less sensitive to extinction. The mid-IR luminosity therefore provides an estimate of the intrinsic AGN power. As such, the presence of absorption in an AGN can be inferred from the observed X-ray to mid-IR luminosity ratio (e.g., Lutz et al. 2004; Alexander et al. 2008; LaMassa et al. 2009; Goulding et al. 2011; LaMassa et al. 2011). We note that the mid-IR emission is also significantly absorbed for $\approx 50\%$ of Compton-thick AGNs (e.g., Bauer et al. 2010; Goulding et al.

2012). Indeed, SDSS J0056+0032 has significant Si-absorption at $9.7\mu\text{m}$, in contrast to SDSS J1157+6003 (see Section 2). To account for this, we have corrected our mid-IR luminosities for dust reddening (see Section 3.3). In Figure 6, we compare the rest-frame X-ray luminosities (L_{X}) of our three Type 2 quasars with the rest-frame $6\mu\text{m}$ luminosities ($L_{6\mu\text{m}}$), exploring both the low-energy (2–10 keV) and high-energy (10–40 keV) X-ray regimes. For SDSS J0011+0056, $L_{2-10\text{keV}}$ was obtained through photometry in the rest-frame 2–10 keV band using *XMM-Newton* data (see Section 3.2). For SDSS J0056+0032 and SDSS J1157+6003, $L_{2-10\text{keV}}$ was obtained through photometry in the observed-frame 0.5–8 keV band using *Chandra* data (see Section 3.2), and an extrapolation to the rest-frame 2–10 keV band assuming a power-law model with $\Gamma = 1.8$. The $L_{10-40\text{keV}}$ values were obtained through a photometric analysis in the rest-frame 10–40 keV band using *NuSTAR* data (see Section 3.1). The $6\mu\text{m}$ luminosities are from SED fitting (Section 3.3) and relate specifically to the emission from the AGN.

In the rest-frame 2–10 keV band, the Type 2 quasars fall below the intrinsic X-ray–mid-IR luminosity relation found for AGNs in the local universe (Lutz et al. 2004); see Figure 6(a). For comparison, we also show the non-beamed sources detected in the *NuSTAR* extragalactic survey (Alexander et al. 2013), which lie within the scatter of the Lutz et al. (2004) relation. The 2–10 keV luminosity suppression of the three Type 2 quasars is expected given our selection and has previously been demonstrated for SDSS J0056+0032 and SDSS J1157+6003 (Vignali et al. 2006, 2010). Assuming the suppression of the X-ray emission is due to absorption, as opposed to intrinsic X-ray weakness, we estimate the column densities of these systems by comparing with the X-ray to mid-IR luminosity ratios for AGNs absorbed by $N_{\text{H}} = 10^{24} \text{ cm}^{-2}$ and $N_{\text{H}} = 5 \times 10^{24} \text{ cm}^{-2}$ (dash-dotted and dashed lines in Figure 6(a), respectively). On the basis of this analysis, the 2–10 keV luminosities of SDSS J0056+0032 and SDSS J1157+6003 are consistent with being absorbed by a factor of $\gtrsim 300$, and therefore lie well within the Compton-thick region with $N_{\text{H}} \gtrsim 5 \times 10^{24} \text{ cm}^{-2}$.

The X-ray emission from SDSS J0011+0056, on the other hand, is suppressed by a factor of ≈ 7 , but is still consistent with being Compton-thick or near Compton-thick ($N_H \approx 10^{24} \text{ cm}^{-2}$). Since our 2–10 keV luminosities were calculated assuming a $\Gamma = 1.8$ power-law, which is probably not consistent with heavy absorption at $z \sim 0.5$, we repeated the flux calculations in Section 3.2 assuming $\Gamma = 0.6$ (the spectral slope of SDSS J0011+0056 as measured by Jia et al. (2013); see Section 2). This results in $L_{2-10 \text{ keV}}$ values which are higher by a factor of ≈ 1.9 ; not enough to significantly change the conclusions drawn from Figure 6(a).

In the rest-frame 10–40 keV band, the X-ray emission is only strongly suppressed for column densities of $N_H \gtrsim 5 \times 10^{24} \text{ cm}^{-2}$, and therefore *NuSTAR* observes the intrinsic X-ray emission for all but the most heavily obscured AGNs; see Figure 6(b). For comparison, Matsuta et al. (2012) studied *Swift*/BAT-detected AGNs and found that for 14–195 keV, only $\approx 60\%$ of Compton-thick objects have significant X-ray suppression with respect to the intrinsic X-ray to mid-IR luminosity ratio. The results in Figure 6(b) suggest that the X-ray emission from SDSS J0011+0056 is not significantly suppressed at 10–40 keV, and is absorbed by $N_H \lesssim 10^{24} \text{ cm}^{-2}$. This is consistent with the X-ray band ratio analysis in Section 4.1. SDSS J0056+0032 is consistent with being Compton-thick, with $N_H \gtrsim 10^{24} \text{ cm}^{-2}$. SDSS J1157+6003 is the strongest candidate for being Compton-thick based on this analysis. Its 10–40 keV luminosity is consistent with being absorbed by a factor of $\gtrsim 10$, despite the high X-ray energies being probed, which again suggests an extreme column density of $N_H \gtrsim 5 \times 10^{24} \text{ cm}^{-2}$. Assuming $\Gamma = 0.6$ rather than $\Gamma = 1.8$ for the *NuSTAR* count rate to flux conversion (Section 3.1.2) results in $L_{10-40 \text{ keV}}$ values which are a higher by a factor of ≈ 1.4 ; again, not enough to significantly change the conclusions drawn from Figure 6(b). As an independent test, we repeated our indirect analyses using [O III] luminosity as a measure of intrinsic AGN power (i.e., using $L_X/L_{[\text{O III}]}$). This yielded very similar results; *NuSTAR* observes the intrinsic X-ray emission of SDSS J0011+0056, while SDSS J0056+0032 and SDSS J1157+6003 are consistent with being heavily Compton-thick ($N_H \gtrsim 5 \times 10^{24} \text{ cm}^{-2}$). However, since our sample was originally selected on the basis of high [O III] luminosity (Zakamska et al. 2003; Reyes et al. 2008), we consider the $L_X/L_{6\mu\text{m}}$ results to be more reliable. Nevertheless, the $L_X/L_{6\mu\text{m}}$ ratio alone is not a robust indicator of Compton-thick absorption, even if the $6\mu\text{m}$ emission accurately reflects the intrinsic power of the AGN. First, some quasars can be intrinsically X-ray weak (e.g., Gallagher et al. 2001; Wu et al. 2011; Luo et al. 2013; Teng et al. 2014). Second, inferred column densities depend on the assumed X-ray spectral model (e.g., Yaqoob & Murphy 2011; Georgantopoulos et al. 2011b). For instance, adding an additional soft scattered component, with a scattering fraction of 2%, to the MYTORUS model predicts a $L_{2-10 \text{ keV}}/L_{6\mu\text{m}}$ ratio for $N_H = 5 \times 10^{24} \text{ cm}^{-2}$ which is a factor of three higher than that shown in Figure 6(b). However, this is not enough to change our broad conclusions regarding the column densities of SDSS J0056+0032 and SDSS J1157+6003. Ultimately, deeper X-ray observations, with simultaneous coverage at low and high energies, are required to directly constrain N_H and provide more robust evidence for or against the presence of Compton-thick absorption in these Type 2 quasars.

5. SUMMARY AND FUTURE WORK

We have presented the first sensitive high-energy ($> 10 \text{ keV}$) analysis of optically selected Type 2 quasars. The sample

consists of three objects that show evidence for Compton-thick absorption ($N_H > 1.5 \times 10^{24} \text{ cm}^{-2}$) on the basis of different diagnostics (see Section 2). Our results can be summarized as follows.

1. One of the Type 2 quasars, SDSS J0011+0056, is detected by *NuSTAR* with 16.8 ± 6.4 counts in the 8–24 keV band. The remaining two, SDSS J0056+0032 and SDSS J1157+6003, are not detected by *NuSTAR*; see Section 3.1.1.
2. For SDSS J0011+0056, we characterize the 3–24 keV spectrum using the X-ray band ratio and find evidence for near Compton-thick absorption with $N_H \gtrsim 5 \times 10^{23} \text{ cm}^{-2}$; see Section 4.1. This is consistent with the column densities inferred from the 2–10 keV to mid-IR ratio, the 10–40 keV to mid-IR ratio, and the X-ray to [O III] ratios; see Section 4.2.
3. For SDSS J0056+0032 and SDSS J1157+6003, we find evidence for a significant suppression of the rest-frame 10–40 keV luminosity with respect to the mid-IR luminosity. If due to absorption, this result implies that these Type 2 quasars are extreme, Compton-thick systems with $N_H \gtrsim 10^{24} \text{ cm}^{-2}$; see Section 4.2.

The characterization of distant heavily obscured AGNs is clearly an extremely challenging pursuit. Nevertheless, as we have demonstrated, the sensitive high-energy observations of *NuSTAR* provide a significant improvement compared to *Chandra* or *XMM-Newton* observations alone; for quasars at $z \sim 0.5$, high column densities of $N_H \gtrsim 5 \times 10^{23} \text{ cm}^{-2}$ can now be directly constrained. Based on the results obtained in this exploratory study, we are now extending the analysis of optically selected Type 2 quasars to a larger sample which is currently being observed by *NuSTAR*. Furthermore, *NuSTAR* is undertaking deep surveys in the ECDFS (J. R. Mullaney et al., in preparation) and COSMOS (F. Civano et al., in preparation) fields, along with a large-area serendipitous survey (Alexander et al. 2013), that are likely to uncover a number of heavily obscured quasars. These upcoming studies will provide a leap forward in our understanding of the column density distribution of distant luminous AGNs.

We acknowledge financial support from the Science and Technology Facilities Council (STFC) grants ST/K501979/1 (G.B.L.), ST/I001573/1 (D.M.A. and A.D.M.) and ST/J003697/1 (P.G.), the Leverhulme Trust (D.M.A. and J.R.M.), Gemini-CONICYT grant 32120009 (R.J.A.), NSF AST award 1008067 (D.R.B.), the International Fulbright Science and Technology Award (M.B.), Basal-CATA PFB-06/2007 (F.E.B.), CONICYT-Chile grant FONDECYT 1101024 (F.E.B.), CONICYT-Chile grant Anillo ACT1101 (F.E.B.), Caltech *NuSTAR* subcontract 44A-1092750 (W.N.B. and B.L.), NASA ADP grant NNX10AC99G (W.N.B. and B.L.), NASA ADAP award NNX12AE38G (R.C.H.), National Science Foundation grant 1211096 (R.C.H.), and Swiss National Science Foundation grant PP00P2_138979/1 (M.K.). We thank the referee for the constructive comments, which helped improve our study. This work was supported under NASA contract No. NNG08FD60C, and made use of data from the *NuSTAR* mission, a project led by the California Institute of Technology, managed by the Jet Propulsion Laboratory, and funded by the National Aeronautics and Space Administration. We thank the *NuSTAR* Operations, Software and Calibration teams for support with the execution and analysis of these observations. This research has made use of the *NuSTAR* Data Analysis Software

(NuSTARDAS) jointly developed by the ASI Science Data Center (ASDC, Italy) and the California Institute of Technology (USA).

REFERENCES

- Alexander, D. M., Chartas, G., Bauer, F. E., et al. 2005, *MNRAS*, **357**, L16
- Alexander, D. M., Chary, R.-R., Pope, A., et al. 2008, *ApJ*, **687**, 835
- Alexander, D. M., Stern, D., Del Moro, A., et al. 2013, *ApJ*, **773**, 125
- Antonucci, R. 1993, *ARA&A*, **31**, 473
- Arnaud, K. A. 1996, in ASP Conf. Ser. 101, *Astronomical Data Analysis Software and Systems V*, ed. G. H. Jacoby & J. Barnes (San Francisco, CA: ASP), 17
- Assef, R. J., Kochanek, C. S., Brodwin, M., et al. 2008, *ApJ*, **676**, 286
- Assef, R. J., Kochanek, C. S., Brodwin, M., et al. 2010, *ApJ*, **713**, 970
- Assef, R. J., Stern, D., Kochanek, C. S., et al. 2013, *ApJ*, **772**, 26
- Bassani, L., Dadina, M., Maiolino, R., et al. 1999, *ApJS*, **121**, 473
- Bauer, F. E., Yan, L., Sajina, A., & Alexander, D. M. 2010, *ApJ*, **710**, 212
- Capri, M., Panessa, F., Bassani, L., et al. 2006, *A&A*, **446**, 459
- Corral, A., Della Ceca, R., Caccianiga, A., et al. 2011, *A&A*, **530**, A42
- Donoso, E., Yan, L., Stern, D., & Assef, R. J. 2013, arXiv:1309.2277
- Draper, A. R., & Ballantyne, D. R. 2010, *ApJL*, **715**, L99
- Fabian, A. C., Vasudevan, R. V., & Gandhi, P. 2008, *MNRAS*, **385**, L43
- Fruscione, A., McDowell, J. C., Allen, G. E., et al. 2006, *Proc. SPIE*, **6270**, 62701V
- Gallagher, S. C., Brandt, W. N., Laor, A., et al. 2001, *ApJ*, **546**, 795
- Gandhi, P., Horst, H., Smette, A., et al. 2009, *A&A*, **502**, 457
- Georgantopoulos, I., Dasyra, K. M., Rovilos, E., et al. 2011a, *A&A*, **531**, A116
- Georgantopoulos, I., Rovilos, E., Akylas, A., et al. 2011b, *A&A*, **534**, A23
- Ghisellini, G., Haardt, F., & Matt, G. 1994, *MNRAS*, **267**, 743
- Gilli, R., Comastri, A., & Hasinger, G. 2007, *A&A*, **463**, 79
- Gilli, R., Vignali, C., Mignoli, M., et al. 2010, *A&A*, **519**, A92
- Goulding, A. D., Alexander, D. M., Bauer, F. E., et al. 2012, *ApJ*, **755**, 5
- Goulding, A. D., Alexander, D. M., Mullaney, J. R., et al. 2011, *MNRAS*, **411**, 1231
- Harrison, F. A., Craig, W. W., Christensen, F. E., et al. 2013, *ApJ*, **770**, 103
- Hasinger, G., Miyaji, T., & Schmidt, M. 2005, *A&A*, **441**, 417
- Hazard, C., Mackey, M. B., & Shimmins, A. J. 1963, *Natur*, **197**, 1037
- Heckman, T. M., Ptak, A., Hornschemeier, A., & Kauffmann, G. 2005, *ApJ*, **634**, 161
- Hopkins, P. F., Hernquist, L., Cox, T. J., & Kereš, D. 2008, *ApJS*, **175**, 356
- Jia, J., Ptak, A., Heckman, T., & Zakamska, N. L. 2013, *ApJ*, **777**, 27
- Kraft, R. P., Burrows, D. N., & Nousek, J. A. 1991, *ApJ*, **374**, 344
- Lacy, M., Storrie-Lombardi, L. J., Sajina, A., et al. 2004, *ApJS*, **154**, 166
- LaMassa, S. M., Heckman, T. M., Ptak, A., et al. 2009, *ApJ*, **705**, 568
- LaMassa, S. M., Heckman, T. M., Ptak, A., et al. 2011, *ApJ*, **729**, 52
- Lawrence, A., Warren, S. J., Almaini, O., et al. 2007, *MNRAS*, **379**, 1599
- Levenson, N. A., Krolik, J. H., Życki, P. T., et al. 2002, *ApJL*, **573**, L81
- Luo, B., Brandt, W. N., Alexander, D. M., et al. 2013, *ApJ*, **772**, 153
- Lusso, E., Hennawi, J. F., Comastri, A., et al. 2013, *ApJ*, **777**, 86
- Lutz, D., Maiolino, R., Spoon, H. W. W., & Moorwood, A. F. M. 2004, *A&A*, **418**, 465
- Maiolino, R., Salvati, M., Bassani, L., et al. 1998, *A&A*, **338**, 781
- Mateos, S., Carrera, F. J., Page, M. J., et al. 2010, *A&A*, **510**, A35
- Matsuta, K., Gandhi, P., Dotani, T., et al. 2012, *ApJ*, **753**, 104
- McCarthy, P. J. 1993, *ARA&A*, **31**, 639
- Meléndez, M., Kraemer, S. B., Armentrout, B. K., et al. 2008, *ApJ*, **682**, 94
- Miley, G., & De Breuck, C. 2008, *A&ARv*, **15**, 67
- Minkowski, R. 1960, *ApJ*, **132**, 908
- Mulchaey, J. S., Koratkar, A., Ward, M. J., et al. 1994, *ApJ*, **436**, 586
- Murphy, K. D., & Yaqoob, T. 2009, *MNRAS*, **397**, 1549
- Netzer, H., Mainieri, V., Rosati, P., & Trakhtenbrot, B. 2006, *A&A*, **453**, 525
- Norman, C., Hasinger, G., Giacconi, R., et al. 2002, *ApJ*, **571**, 218
- Osterbrock, D. E. 1981, *ApJ*, **249**, 462
- Panessa, F., Bassani, L., Capri, M., et al. 2006, *A&A*, **455**, 173
- Pâris, I., Petitjean, P., Aubourg, É., et al. 2012, *A&A*, **548**, A66
- Ptak, A., Zakamska, N. L., Strauss, M. A., et al. 2006, *ApJ*, **637**, 147
- Reyes, R., Zakamska, N. L., Strauss, M. A., et al. 2008, *AJ*, **136**, 2373
- Risaliti, G., Maiolino, R., & Salvati, M. 1999, *ApJ*, **522**, 157
- Roseboom, I. G., Lawrence, A., Elvis, M., et al. 2013, *MNRAS*, **429**, 1494
- Salpeter, E. E. 1964, *ApJ*, **140**, 796
- Sanders, D. B., Soifer, B. T., Elias, J. H., et al. 1988, *ApJ*, **325**, 74
- Schmidt, M. 1963, *Natur*, **197**, 1040
- Scott, A. E., Stewart, G. C., Mateos, S., et al. 2011, *MNRAS*, **417**, 992
- Shi, Y., Rieke, G. H., Hines, D. C., et al. 2006, *ApJ*, **653**, 127
- Soltan, A. 1982, *MNRAS*, **200**, 115
- Steffen, A. T., Strateva, I., Brandt, W. N., et al. 2006, *AJ*, **131**, 2826
- Steidel, C. C., Hunt, M. P., Shapley, A. E., et al. 2002, *ApJ*, **576**, 653
- Stern, D., Assef, R. J., Benford, D. J., et al. 2012, *ApJ*, **753**, 30
- Stern, D., Eisenhardt, P., Gorjian, V., et al. 2005, *ApJ*, **631**, 163
- Stern, D., Moran, E. C., Coil, A. L., et al. 2002, *ApJ*, **568**, 71
- Teng, S. H., Brandt, W. N., Harrison, F. A., et al. 2014, *ApJ*, in press (arXiv:1402.4811)
- Treister, E., & Urry, C. M. 2005, *ApJ*, **630**, 115
- Treister, E., Urry, C. M., & Virani, S. 2009, *ApJ*, **696**, 110
- Turner, T. J., George, I. M., Nandra, K., & Mushotzky, R. F. 1997, *ApJ*, **488**, 164
- Ueda, Y., Akiyama, M., Ohta, K., & Miyaji, T. 2003, *ApJ*, **598**, 886
- Urry, C. M., & Padovani, P. 1995, *PASP*, **107**, 803
- Vanden Berk, D. E., Richards, G. T., Bauer, A., et al. 2001, *AJ*, **122**, 549
- Véron-Cetty, M.-P., & Véron, P. 2010, *A&A*, **518**, A10
- Vignali, C., Alexander, D. M., & Comastri, A. 2006, *MNRAS*, **373**, 321
- Vignali, C., Alexander, D. M., Gilli, R., & Pozzi, F. 2010, *MNRAS*, **404**, 48
- Vignali, C., Comastri, A., Stirpe, G. M., et al. 1998, *A&A*, **333**, 411
- Weisskopf, M. C., Wu, K., Trimble, V., et al. 2007, *ApJ*, **657**, 1026
- Wright, E. L., Eisenhardt, P. R. M., Mainzer, A. K., et al. 2010, *AJ*, **140**, 1868
- Wu, J., Brandt, W. N., Hall, P. B., et al. 2011, *ApJ*, **736**, 28
- Yaqoob, T., & Murphy, K. D. 2011, *MNRAS*, **412**, 835
- York, D. G., Adelman, J., Anderson, J. E., Jr., et al. 2000, *AJ*, **120**, 1579
- Zakamska, N. L., Gómez, L., Strauss, M. A., & Krolik, J. H. 2008, *AJ*, **136**, 1607
- Zakamska, N. L., Strauss, M. A., Heckman, T. M., Ivezić, Ž., & Krolik, J. H. 2004, *AJ*, **128**, 1002
- Zakamska, N. L., Strauss, M. A., Krolik, J. H., et al. 2003, *AJ*, **126**, 2125